# Supplementary Materials

## Hierarchical Nanolattice Design

The hierarchical nanolattices fabricated in this work are designed using a recursive method that combines different unit cells into hierarchical geometries. The design process takes place as follows: 1) two (unique or identical) unit cell geometries are prescribed, 2) one unit cell is designated 1st order and the other 2nd order, and 3) the 1st order unit cell is patterned along the length of the 2nd order unit cell with *N* repeating units, resulting in a fractal-like geometry (Fig. S1). These steps can be repeated iteratively to create a fractal of any order, and the method is sufficiently general that it can be repeated for a wide range of unit cell geometries (Fig. S2). For the samples tested in this work, 1st order axial support beams were added along the length of the 2nd order beam to ensure that the hierarchical beams formed a stretching-dominated geometry.

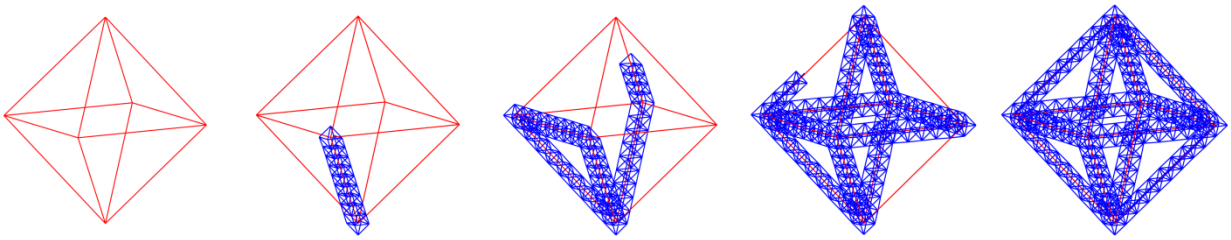

***Figure S1****: Hierarchical nanolattice design project showing the construction of an octahedron-of-octahedra unit cell.*

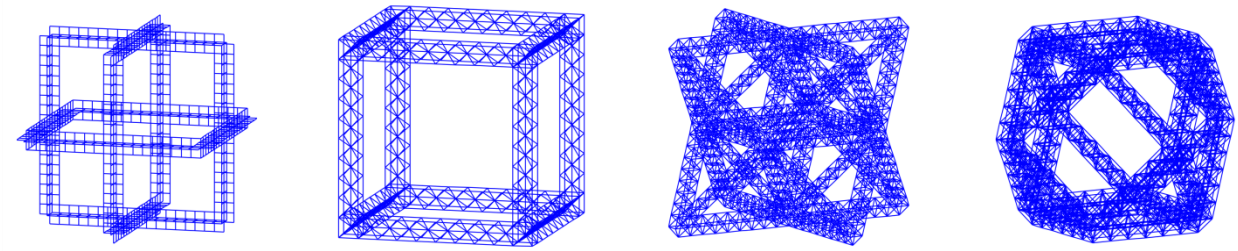

***Figure S2****: Hierarchical nanolattice geometries showing the versatility of the design process. The different geometries shown are: a) a cage of crosses, b) a cube of reinforced-BCC unit cells, c) an octet-truss of octahedra, and d) a cuboctahedron of embedded-octahedra.*

## Fabrication Details

Hierarchical nanolattices were fabricated out of solid polymer, polymer-ceramic core-shell composite, and hollow ceramic. There are three unique steps involved in the fabrication of these samples: 1) writing of a polymer sample, 2) coating of that polymer sample with a ceramic thin film, and 3) removal of the polymer. Each material system tested in this work represents one of the steps involved in the fabrication process.

Fabrication of all samples begins with the writing of a polymer sample out of photoresist (IP-Dip 780) using two-photon lithography (TPL) direct laser writing (DLW) in a Photonic Professional DLW system (Nanoscribe GmbH). Samples are written using laser powers in a range from 6-12mW and a writing speed of ~50µm/s. The minimum writing spot size (voxel) is an ellipsoid with a width between 150-600nm and approximately a 4:1 height to width aspect ratio. The laser power is used to control the

diameter of the tubes, and the speed varies slightly during the writing process to control the quality of the structure. In the samples, individual 1$^{st}$ order beams are written with three lines – one central line and one on either side with a 150μm offset perpendicular to the axis of the beam – to reduce the ellipticity of the beam.

After a polymer scaffold is written, samples are conformally coated with 20nm of aluminum oxide (alumina) using atomic layer deposition (ALD). Deposition is done at 150°C in a Cambridge Nanotech S200 ALD system using the following steps: $H_2O$ is pulsed for 15ms, the system is purged for 20s, trimethyl aluminum (TMA) is pulsed for 15ms, the system is purged for 20s, and the process is repeated. The carrier gas is nitrogen, which is used at a flow rate of 20sccm (standard cubic centimeters per minute). The process was repeated for 200 cycles to obtain the desired thickness coating. The thickness of the coatings was verified using spectroscopic ellipsometry with an alpha-SE Ellipsometer (J.A. Wollam Co., Inc.).

After deposition, a focused ion beam (FIB) (Versa 3D DualBeam, FEI) is used to mill away selected regions of the sample to expose the polymer to air. Once the polymer is exposed, samples are placed into an $O_2$ plasma etcher (Zepto, Diener GmbH) for between 30-60 hours at a pressure of 0.5 mbar and at 100W of power in order to fully remove the polymer. It is possible to determine whether the polymer has been fully etched away by looking for any contrast change in the beams using a scanning electron microscope (1).

**Polymer Constituent Properties**

Mechanical characterization of the IP-Dip polymer was performed through micropillar compression experiments in a nanomechanical testing device (TI 950 Triboindenter, Hysitron Inc.). Micropillars were compressed using a 20μm diamond flat punch tip to 10-15% strain at a rate of $10^{-3}$ $s^{-1}$ then held at their peak displacement for 50 s before unloading. Samples were fabricated out of IP-Dip photoresist using an identical DLW method to that described above for hierarchical nanolattices. Samples were fabricated and tested with diameters between 2-10μm, and length-to-diameter (L/D) ratios between 2 and 4.

For each micropillar, stress-strain data was obtained and used to determine the Young's modulus ($E$) and compressive yield strength ($\sigma_y$). The Young's modulus is calculated using the slope of the linear regime of the stress-strain curve. The compressive yield strength is calculated by finding the intersection of the stress-strain data with a 0.2% strain offset curve from the linear regime. Three representative data sets along with their corresponding yield strength and stiffnesses are shown in Figure S3. The stress-strain data has an initial toe region followed by a linear regime and then a plastic flow region. The toe region is likely due to improper alignment or contact of the indenter tip with the sample, and was consequently ignored in the calculation of the Young's modulus. Based on the stress-strain data, we found that the IP-Dip polymer had an average modulus of $\boldsymbol{E = 2.1 \pm 0.3\ GPa}$ and an average yield strength of $\boldsymbol{\sigma_y = 67.2 \pm 4.7\ MPa}$ (Fig. S3).

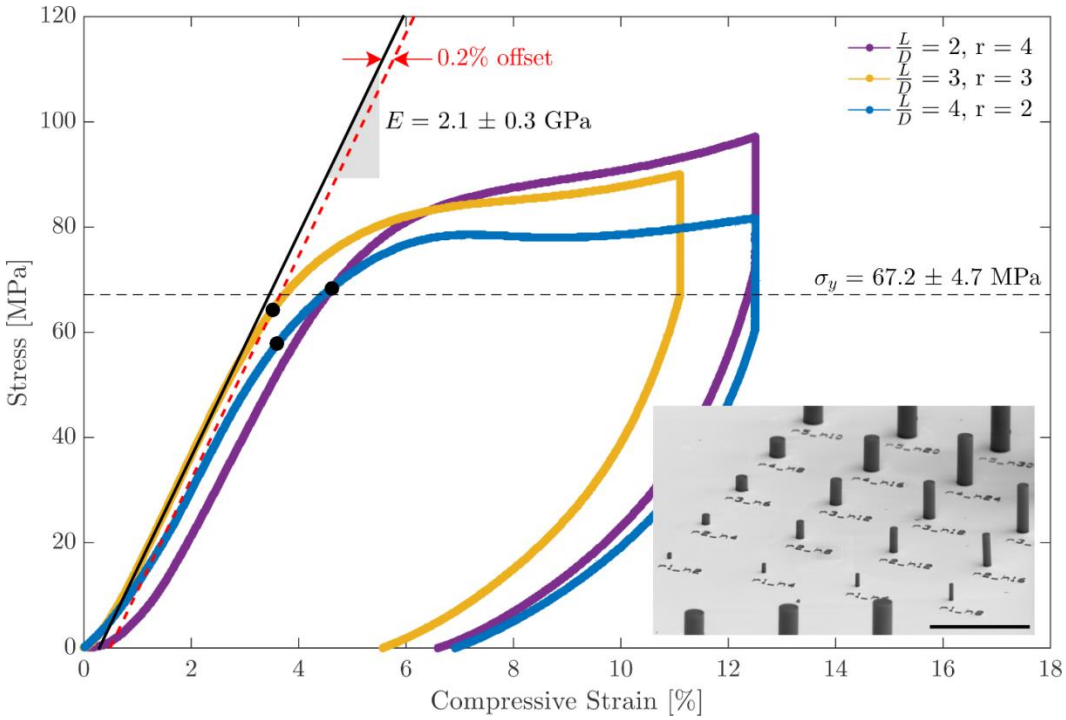


***Figure S3**: Representative stress-strain data for each slenderness ratio tested (L/D = 2, 3, 4) with various radii. The arithmetic mean of the Young's modulus (E) and compressive yield strength ($\sigma_y$) are plotted. The inset image shows a set of pre-compression micropillar samples (scale bar: 50 µm).*

**Composite Constituent Properties**

The properties of the composite were calculated using a Voigt model rule of mixtures, with the properties of the ALD $Al_2O_3$ taken from (Refs. 2–6). In the 2nd order half cells, the polymer beams have dimensions of $a = 753nm$ and $b = 317nm$, where $a$ and $b$ are the major and minor radii of the ellipse, respectively. The ceramic shell has a thickness of $t = 20nm$; the volume fraction of polymer in the beams can be calculated to be $f = A_{polymer}/(A_{polymer} + A_{ceramic}) = 91.6\%$. Given the polymer properties of $E_p = 2.1 \pm 0.3\ GPa$ and $\sigma_{yp} = 67.2 \pm 4.7\ MPa$, and the ceramic properties of $E_h = 165\ GPa$ and $\sigma_{yh} = 5.2\ GPa$, we can obtain the core shell composite properties to be $fE_p + (1-f)E_h = \boldsymbol{E_c = 15.8\ GPa}$ and $f\sigma_{yp} + (1-f)\sigma_{yh} = \boldsymbol{\sigma_{yc} = 509\ MPa}$.

**Relative Density Calculations**

The relative density of each hierarchical sample was determined using a representative CAD model (SOLIDWORKS, Dassault Systèmes). The model enabled quick calculations for solid and hollow samples. Figure S4 illustrates the design process of the CAD model.

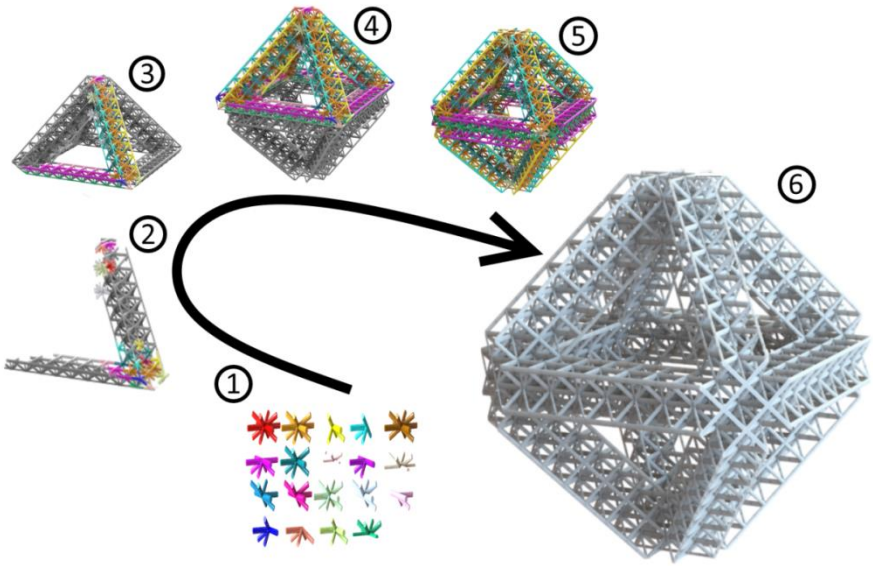


***Figure S4****: Illustration of the design approach used to construct a CAD model. The above images show the construction of a 2nd order octahedron-of-octets unit cell. (1) Unique nodes that make up the unit cell. (2) Nodes are minimally patterned to create a unit cell beam. (3-4) Assembled nodes are patterned to create the full geometry. (5) Boundaries are cut to form the unit cell. (6) Finished unit cell whose volume properties can be measured.*

**Failure Mode Formulation**

Failure in hierarchical nanolattices primarily initiated in 1st order beams. In polymer samples, failure occurs via beam (Euler) buckling, while in composite samples failure occurs via brittle fracture. The continuous and serrated flow behavior of the hollow nanolattices indicates the occurrence of Euler buckling and shell buckling, the combination of which gives rise to a ductile-like deformation with a near 100% recovery. Large drops in the stress generally correspond to large Euler buckling events; smaller drops are more likely to coincide with localized shell buckling events. The failure criterion for beam buckling and shell buckling in an elliptical beam with a semi-major axis $a$, semi-minor axis $b$, thickness $t$, and length $L$ are

$$\sigma_{beam} = \frac{\pi^2 EI}{(kL)^2 A} \approx \frac{\pi^2 E\left(\frac{3\pi}{4}ab^2t\right)}{L^2\left(\pi t(a+b)\right)} = \frac{3\pi^2 E}{4L^2}\frac{ab^2}{a+b} \quad \textbf{(S1)}$$

$$\sigma_{shell} = \frac{E}{\sqrt{3(1-\nu^2)}}\left(\frac{t}{a}\right) \quad \textbf{(S2)}$$

Here, $E$ is the Young's modulus and $\nu$ is the Poisson's ratio of the material. By equating the failure criterion for beam buckling and shell buckling, it is possible to find a transition between the two. Here, we quantify the transition using a critical dimensionless parameter $SB$ as

$$\frac{3\pi^2 E}{4L^2}\frac{ab^2}{a+b} = \frac{E}{\sqrt{3(1-\nu^2)}}\left(\frac{t}{a}\right) \quad \textbf{(S3)}$$

$$\boxed{SB = \left(\frac{t(a+b)L^2}{a^2b^2}\right)_{cr} = \frac{3\pi^2}{4}\sqrt{3(1-\nu^2)} \approx 12.2} \quad \textbf{(S4)}$$

If the critical buckling transition value for a beam is $SB \leq 12.2$, shell buckling will be the dominant failure mechanism over beam buckling, and if $SB > 12.2$, beam buckling will be the dominant failure mechanism. In the hollow samples tested in this work, the $SB$ values range from 14.8 to 33.3, meaning that all the samples tested here are in a beam buckling failure mode regime.

Previous work by Meza et. al. reported that hollow $Al_2O_3$ nanolattices exhibit ductile-like behavior with near complete recoverability when the wall-thickness-to-tube-radius ratio is below a critical transition value of $\left(\frac{t}{a}\right)_{cr} = \frac{\sigma_{fs}}{E}\sqrt{3(1-\nu^2)} \approx 0.03$, where $\sigma_{fs}$ is the fracture strength of the constituent material (1). All samples tested in this work have $\left(\frac{t}{a}\right) < 0.03 < \left(\frac{t}{a}\right)_{cr}$, meaning that shell buckling will take place preferentially over yielding. This analytical formulation shows that in the 1st order beams, beam buckling will take place preferentially over shell buckling, and after the occurrence of beam buckling, shell buckling will take place over fracture, allowing samples to deform in a ductile-like manner and accommodate large strains. This matches very closely to what is observed experimentally.

**Full Hierarchical Nanolattice Mechanical Behavior**

2nd order full hierarchical nanolattices were fabricated in a 3x3x3 array using octahedra-of-octahedra hierarchical unit cells. Samples were compressed using an in-situ nanoindenter at a strain rate of $10^{-3}$ $s^{-1}$ to 50% strain in a manner nearly identical to the half-cell samples. Failure mechanisms in the 2nd order full nanolattices closely matched those in the 2nd order half-cells for each material type: polymer samples underwent ductile failure via beam buckling, composite samples underwent catastrophic brittle collapse via fracture of the constituent $Al_2O_3$, and hollow samples underwent serrated ductile-like failure via a combination of beam buckling and shell buckling.

The stiffness and strength of the hierarchical nanolattice samples closely matched that of the half-cell samples, and a full list of results can be found in Figure S5. The primary distinction between the failure of the full samples and the half-cell samples is the emergence of a layer-by-layer collapse deformation mechanism, which led to high local stresses in the beams and reduced the recoverability in the full nanolattices compared with the half-cell samples. 2nd order polymer nanolattices recovered immediately to 65-85% of their original height, with additional viscoelastic recoveries of 5-20% after unloading. 2nd order composite nanolattices had a catastrophic strain burst with failure localized to the top of the lattice and exhibited little to no recovery. 2nd order hollow nanolattices had layer-by-layer deformation that limited their recovery to only 60-75% of the original height, compared with 85-98% in the equivalent hollow half-cell samples.

In hollow samples, the layer-by-layer collapse generated local highly strained regions where the buckled beams partially fractured without complete failure. The bifurcated beams experienced marginal recovery due to the residual strain energy being insufficient to return the sample to its original

configuration. Preventing layer-by-layer collapse would improve recovery but requires a more efficient hierarchical geometry to optimize load distribution.

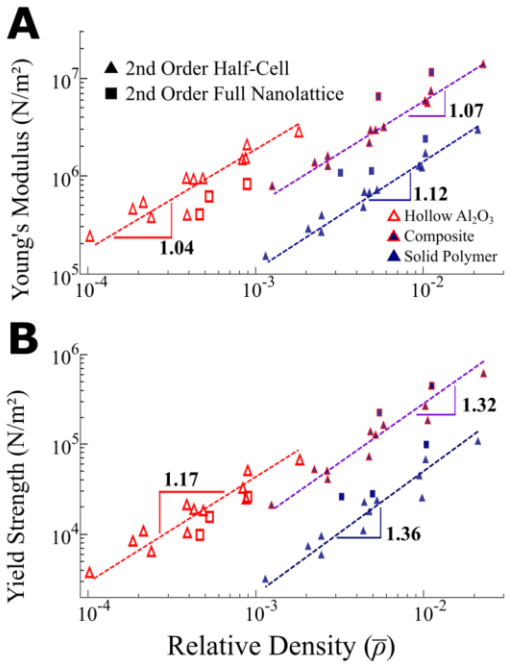


***Figure S5:*** *Comparison of mechanical data of 2nd order half-cells against full hierarchical nanolattices showing their close agreement for (a) Young's modulus vs. relative density and (b) yield strength vs. relative density.*

## Effect of Slenderness on Deformation

Samples with a range of structural parameters and slenderness ratios were tested in this work. We show a number of representative samples of different material systems demonstrating the deformation and failure modes of samples with high and low slenderness in Figure S6 below.

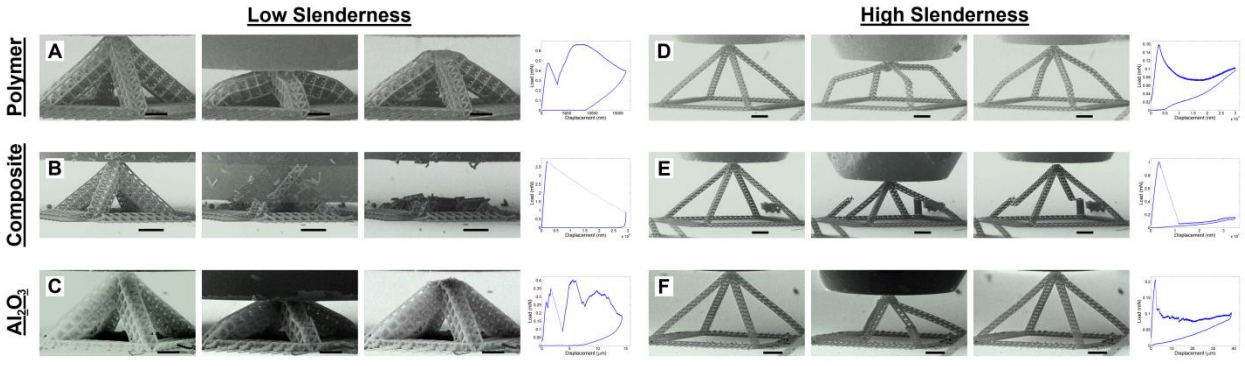


***Figure S6:*** *Compression experiments performed on 2nd order half-cells showing the samples in an undeformed configuration, at 50% strain, and unloaded, along with the corresponding load (mN) v displacement (μm) data. All 'high slenderness' samples are octahedra-of-octahedra and all 'low slenderness' samples are octahedra-of-octets. Samples* a-c *have* $L = 8\mu m$ *and* $N = 10$*, and samples* d-f *have* $L = 12\mu m$ *and* $N = 20$*. Samples* ***A*** *and* ***D*** *are pure polymer,* ***B*** *and* ***E*** *are polymer-ceramic core-shell composites, and* ***C*** *and* ***F*** *are hollow* $Al_2O_3$*.*

**FEM Modeling**

Modeling hierarchical lattices is a computationally demanding problem because the problem size scales exponentially. To reduce problem size one can use either a simplistic method or an adaptive method. The first, simplistic method uses bar elements in the Truss Model. Bar elements are the simplest and computationally least expensive method of modeling lattices. Our simple refined model is significantly more complex but can adaptively scale with the level of hierarchy through repeated use of substructure generation and utilization.

Two modeling approaches were used to predict lattice stiffness and stress distributions. The first approach uses an in-house finite element code with small-strain bar elements having only axial stiffness. A linear elastic material model is assumed to govern the bar response. Figure S7 shows an example truss structure with the half-cell bottom fully constrained and the vertical displacements imposed on the top nodes of the cell. Vertical reaction forces were calculated at the top nodes to determine the lattice stiffness.

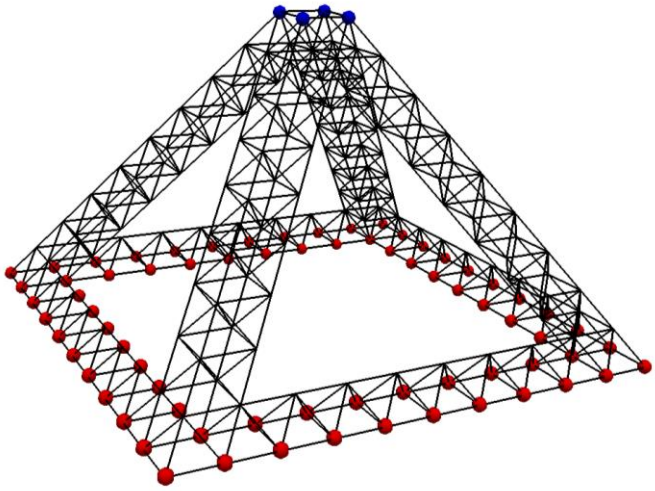

***Figure S7****: Truss model of half-cell octahedron of octahedrons with applied boundary conditions: red – all translation DOF constrained, blue – prescribed vertical displacement.*

In contrast to the first model approach, the second, referred to as the refined model, is a scalable solution to modeling hierarchical lattices by using degree-of-freedom (DOF) condensation. The refined model consists of two stages: substructure generation and substructure utilization. *Substructure generation* begins with identifying the geometrically unique nodes and beams (Fig. 4).

For compatibility between nodes and beams generalized DOFs, referred to as compatibility DOF, are introduced at the center of each node- and beam-connecting edge or face and the latter are assumed to deform rigidly; e.g. the end faces of each beam deform rigidly so that their motion can be described solely by its compatibility DOFs (i.e., its generalized translational and rotational DOFs). A substructure condensation method is applied to each beam or node part such that the only remaining DOFs are the compatibility DOFs. *Substructure utilization* then extracts the effective stiffness matrices of all

substructure parts, assembles those accordingly into a hierarchical half-cell lattice, and couples the compatibility DOF of each substructure to the appropriate adjacent substructure (Fig. 4D and E).

Substructure generation and utilization can be performed repeatedly on increasingly larger levels of hierarchy to reduce the computational cost of evaluating the final lattice stiffness. Also, the extraction of the effective beam and node response from full-scale finite element models of the latter can be performed a priori so there is no need to recover full-resolution simulations during the final simulation run.

Two general trends are observed for solid and hollow lattices. First, solid lattice stiffness predicted by the simple truss model is generally less than that of the refined model. Secondly, hollow lattice stiffness predicted by the truss model is greater than that of the refined model. These differences arise because of the contributions of bending and node junctions to degrading the overall lattice stiffness in the refined model. Figure S8 summarizes computational and experimental stiffness data and compares the simulated stiffnesses obtained from each model for geometrically perfect lattices. The refined model more accurately predicts properties of solid polymer and hollow ceramic lattice stiffness by 5.0 and 1.4 times, respectively, relative to the truss predictions. In simulating composites nanolattices, the truss model is 1.4 times more accurate than the refined model. If one takes into account geometric imperfections of the nanolattices, such as the beam waviness, the predicted stiffness of both the refined model and the truss model would decrease such that the refined model is always more accurate than the truss model relative to experimental data.

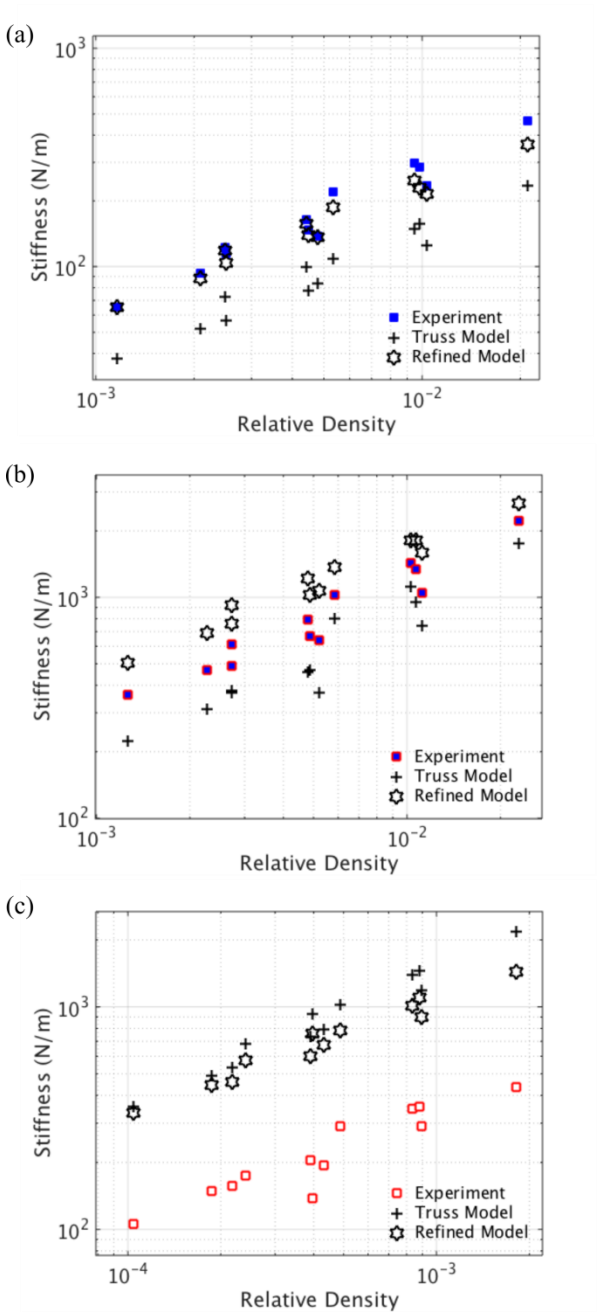


***Figure S8:*** *Comparison of model approximations and experimental data of second order half-cell lattices consisting of (a) solid polymer, (b) solid polymer with ceramic coating, (c) hollow ceramic.*

## Complete List of Samples Tested

| Composition | Geometry | Unit Cell Size (μm) | Fractal Number | Relative Density |
|---|---|---|---|---|
| Solid Polymer | Octahedron-of-Octahedra | 8 | 10 | 1.03E-2 |
| | | 8 | 15 | 4.49E-3 |
| | | 8 | 20 | 2.50E-3 |
| | | 12 | 10 | 4.80E-3 |
| | | 12 | 15 | 2.09E-3 |
| | | 12 | 20 | 1.16E-3 |
| | Octahedron-of-Octets | 8 | 10 | 2.10E-2 |
| | | 8 | 15 | 9.46E-3 |
| | | 8 | 20 | 5.34E-3 |
| | | 12 | 10 | 9.82E-3 |
| | | 12 | 15 | 4.41E-3 |
| | | 12 | 20 | 2.49E-3 |
| Composite | Octahedron-of-Octahedra | 8 | 10 | 1.12E-2 |
| | | 8 | 15 | 4.88E-3 |
| | | 8 | 20 | 2.72E-3 |
| | | 12 | 10 | 5.23E-3 |
| | | 12 | 15 | 2.28E-3 |
| | | 12 | 20 | 1.27E-3 |
| | Octahedron-of-Octets | 8 | 10 | 2.28E-2 |
| | | 8 | 15 | 1.03E-2 |
| | | 8 | 20 | 5.83E-3 |
| | | 12 | 10 | 1.07E-2 |
| | | 12 | 15 | 4.81E-3 |
| | | 12 | 20 | 2.73E-3 |
| Hollow $Al_2O_3$ | Octahedron-of-Octahedra | 8 | 10 | 8.95E-4 |
| | | 8 | 15 | 3.90E-4 |
| | | 8 | 20 | 2.17E-4 |
| | | 12 | 10 | 4.30E-4 |
| | | 12 | 15 | 1.87E-4 |
| | | 12 | 20 | 1.04E-4 |
| | Octahedron-of-Octets | 8 | 10 | 1.82E-3 |
| | | 8 | 15 | 8.36E-4 |
| | | 8 | 20 | 4.89E-4 |
| | | 12 | 10 | 8.78E-4 |
| | | 12 | 15 | 3.95E-4 |
| | | 12 | 20 | 2.41E-4 |

***Table S1**: Full list of fabricated 2nd order half-cell geometries with corresponding relative densities*

| Composition | Unit Cell Size (μm) | Fractal Number | Relative Density |
|---|---|---|---|
| Solid Polymer | 8 | 5 | 2.32E-2 |
| | 3 | 10 | 3.55E-3 |
| Composite | 8 | 5 | 1.83E-2 |
| | 8 | 5 | 2.51E-2 |
| | 3 | 10 | 2.15E-3 |
| Hollow $Al_2O_3$ | 8 | 5 | 1.83E-3 |
| | 3 | 10 | 4.73E-4 |

***Table S2**: Full list of fabricated 3rd order octahedron half-cell geometries with corresponding relative densities*

| Composition | Unit Cell Size (μm) | Fractal Number | Relative Density |
|---|---|---|---|
| Solid Polymer | 8 | 10 | 1.03E-2 |
| | 6 | 15 | 4.95E-3 |
| | 4 | 20 | 3.26E-3 |
| Composite | 8 | 10 | 1.12E-2 |
| | 6 | 15 | 5.49E-3 |
| Hollow $Al_2O_3$ | 8 | 10 | 8.95E-4 |
| | 6 | 15 | 5.35E-4 |
| | 4 | 20 | 4.71E-4 |

***Table S3**: Full list of fabricated 2nd order octahedron full-lattice geometries with corresponding relative densities*

**References**


1. Meza LR, Das S, Greer JR (2014) Strong, lightweight, and recoverable three-dimensional ceramic nanolattices. *Science* 345(6202):1322–1326.

2. Berdova M, et al. (2014) Mechanical assessment of suspended ALD thin films by bulge and shaft-loading techniques. *Acta Mater* 66:370–377.

3. Ilic B, Krylov S, Craighead HG (2010) Young's modulus and density measurements of thin atomic layer deposited films using resonant nanomechanics. *J Appl Phys* 108:1–11.

4. Jen S-H, Bertrand JA, George SM (2011) Critical tensile and compressive strains for cracking of Al2O3 films grown by atomic layer deposition. *J Appl Phys* 109(8):084305.

5. Tripp MK, et al. (2006) The mechanical properties of atomic layer deposited alumina for use in micro- and nano-electromechanical systems. *Sensors Actuators A Phys* 130-131:419–429.

6. Bauer J, et al. (2015) Push-to-pull tensile testing of ultra-strong nanoscale ceramic–polymer composites made by additive manufacturing. *Extrem Mech Lett*.